Processing and characterization of Ultra High Temperature High-Entropy $(Ti_{0.2}Zr_{0.2}Hf_{0.2}Mo_{0.2}W_{0.2})B_2$-based Ceramics: Effect of W granulometry, graphite, and SiC addition

Mariano Casu [a], Simone Barbarossa [a], Antonio M. Locci [a], Giacomo Cao [a], Costantino Cau [b], Laura Caggiu [b], Sebastiano Garroni [b], Paolo Ferro [c], Roberto Orrù [a,*]

[a] Department of Mechanical, Chemical, and Materials Engineering, Research Unit of the National Interuniversity Consortium of Materials Science and Technology (INSTM), University of Cagliari, via Marengo 2, Cagliari 09123, Italy
[b] Department of Chemical, Physical, Mathematical, and Natural Sciences, University of Sassari, Sassari 07100, Italy
[c] Department of Management and Engineering, University of Padova, Stradella S. Nicola 3, Vicenza 36100, Italy

ARTICLE INFO

ABSTRACT

A highly dense and single phase $(Ti_{0.2}Zr_{0.2}Hf_{0.2}Mo_{0.2}W_{0.2})B_2$ ceramic product is obtained in this work at 1950°C (20 min, 20 MPa) by Spark Plasma Sintering (SPS) from powders prepared by Self-propagating High-temperature Synthesis (SHS). The formation of the $(W,Mo)B_2$ secondary phase is avoided using fine W precursors and adding 1 wt% graphite to the SHS powders before SPS. Kinetic limitations responsible for hindering the synthesis of the high entropy boride are correspondingly eliminated. The resulting 98.5 % dense sample exhibits a homogeneous microstructure, with Vickers hardness of 26.8 GPa. The introduction of 20 vol% SiC produces an increase of the K_{IC} values from 2.32 to 5.11 MPa m$^{1/2}$. Very relevant is that the volatilization of Mo- and W-oxides occurring during sample oxidation at high temperature, which leads to its rapid degradation with the formation of a very porous oxide scale, can be strongly inhibited by the silicate phases generated in the composite ceramic.

1. Introduction

In the last decade, the application of the High Entropy paradigm to transition metal diborides and carbides, produced a marked increase of the members which fall within the general class of Ultra High Temperature Ceramics (UHTCs) [1,2]. In this context, a growing interest was addressed to quinary high entropy transition metal diborides (HEBs), fabricated for the first time in bulk form by Gild et al. [3], resulting from the combination in near-equimolar ratio of five individual constituents (HfB$_2$, ZrB$_2$, TiB$_2$, etc.) to form crystalline solid solutions with maximum configurational entropy. As for standard UHTCs, these multicomponent ceramics are potentially attractive in several application fields, including the aerospace, nuclear industry, as solar energy absorbers, etc. [1,2,4–6].

Few attempts, usually failed, have been made to produce dense HEBs or other multicomponent borides by reactive sintering from raw powders, with no preliminary treatment but their mixing [7–9]. As an exception, the synthesis of the medium-entropy $(W_{1/3}Re_{1/3}Ru_{1/3})B_2$ system was successfully obtained directly by SPS starting from high

purity W, Re, Ru and B powders [9]. The $(Hf_{0.2}Zr_{0.2}Ta_{0.2}Nb_{0.2}Ti_{0.2})$ B$_2$-SiC ceramic composite was also prepared by reactive Spark Plasma Sintering using the corresponding high-entropy carbide, B$_4$C and Si as starting materials [10].

More often, their fabrication is carried out in two processing steps. Powders synthesis, or the activation of initial precursors, is carried out during the first stage generally using High Energy Ball Milling (HEBM) [3,11–16], borothermal (BT) [17] or boro-carbothermal reduction (BCR) [18–21] of metal oxides, and Self-propagating High temperature Synthesis (SHS) [7,8,22,23]. Other techniques, for instance liquid phase methods, are also proposed for powder preparation [24]. The second step, aimed to the fabrication of dense bodies, is commonly performed by Spark Plasma Sintering (SPS). After optimization of the operating conditions, the methods above often succeeded in the obtainment of several dense quinary borides, like for example $(Ti_{0.2}Hf_{0.2}Nb_{0.2}Ta_{0.2}Mo_{0.2})B_2$, $(Ti_{0.2}Zr_{0.2}Hf_{0.2}Ta_{0.2}Mo_{0.2})B_2$, $(Ti_{0.2}Zr_{0.2}Hf_{0.2}Nb_{0.2}Mo_{0.2})$ B$_2$, etc., as single-phase solid solutions [18–23]. For the sake of clarity, the rule of the "IVB-VIB group sequence" has been used in this work for writing the chemical formula of HEBs, even though the transition metals

---

* Corresponding author.
  E-mail address: roberto.orru@unica.it (R. Orrù).

involved can be found ordered differently in the literature. In this context, the several efforts made to synthesize the $(Ti_{0.2}Zr_{0.2}Hf_{0.2}Mo_{0.2}W_{0.2})B_2$ system often result in multiple phase products [3,17,18, 21]. Results reported in literature relative to $(Ti_{0.2}Zr_{0.2}Hf_{0.2}Mo_{0.2}W_{0.2})$ B_2-based ceramics prepared in bulk form are summarized in Table 1, along with the corresponding preparation routes, processing conditions, and samples density. In the latter regard, it is worth pointing out that no data could be found on SiC-containing products, relatively to this specific HEB system.

For instance, a 6 h HEBM treatment of metal borides followed by SPS process provided sample with a W-rich secondary phase, ascribed to $(Ti_{1.6}W_{2.4})B_4$ [3]. The presence of a secondary (W,Mo)-rich phase was detected in the sintered materials when the same authors combined BCR and SPS routes [18]. Similarly, WB was the additional phase found, along with the desired HEB, in the final product obtained by **Zhang et al.** [17] using the BT-SPS approach. Secondary phases, including (W, Mo)B_2, were also detected in the ceramic produced by Pressureless Sintering (PLS) from HEB-based powders synthesized by BCR [21].

Apparently, only few investigations succeeded so far in the obtainment of the single phase $(Ti_{0.2}Zr_{0.2}Hf_{0.2}Mo_{0.2}W_{0.2})B_2$ ceramic [11,19, 20]. In particular, while the SPS product obtained from a mixture of metal borides previously treated by HEBM also contained a W-rich monoboride byproduct, which was ascribed to $(W_{0.78}Mo_{0.19}Ti_{0.02}Hf_{0.01})$ B, no secondary phases were detected using elemental precursors co-milled for 50 min (ball to powder weight ratio, BPR=4) prior to RSPS (multistep process, 2000°C/10 min/50 MPa, as final condition) [11]. A similar achievement was reported by **Monteverde et al.** [19], who combined the BCR route (HfO_2, ZrO_2, TiO_2, MoO_3, WO_3, B_4C, and carbon black, as raw materials) with the SPS process (2000°C/10 min/50 MPa), to provide a dense product, containing only some residual reactants (B_4C+C, about 2.5 vol%) in addition to the expected one.

Apart from the difficulties associated to their fabrication, other crucial issues concerning HEBs are, as for standard metal diborides, their scarce mechanical properties, particularly fracture toughness, and their

modest oxidation resistance at high temperatures [8,25–27]. In the latter regard, following the positive effect obtained with the introduction of Si-containing additives (SiC, $TaSi_2$, $MoSi_2$, etc.) to individual borides, some investigations focused on the fabrication and characterization of HEBs-SiC systems have been recently conducted [8,28–32]. For instance, it was reported that the addition of 20 vol%SiC to $(Ti_{0.2}Zr_{0.2}Hf_{0.2}Nb_{0.2}Ta_{0.2})B_2$ powders produced by BCR favored sample consolidation, and the obtained product was characterized by a finer microstructure and superior fracture toughness with respect to the additive free counterpart [28,29]. The HEB system above, once combined with different amounts (10, 20, 30 %vol.) of SiC, was also investigated by **Cheng et al.** [32]. The main effects produced by the carbide additive were HEB grain growth inhibition, powders consolidation enhancement, and improvement of mechanical properties (Vickers hardness and fracture toughness). More recently, bulk $(Ti_{0.2}Hf_{0.2}Nb_{0.2}Ta_{0.2}Mo_{0.2})B_2$ −27.7 vol%SiC and $(Ti_{0.2}Zr_{0.2}Hf_{0.2}Ta_{0.2}Mo_{0.2})B_2$-27.4 vol%SiC composites were produced by SPS from powders synthesized by SHS from elemental transition metals, B_4C and Si precursors [8]. Significant benefits, in terms of sintering behavior, mechanical properties, and oxidation resistance at high temperatures, were clearly gained in presence of SiC.

In this work, the synthesis of dense $(Ti_{0.2}Zr_{0.2}Hf_{0.2}Mo_{0.2}W_{0.2})B_2$ is accomplished for the first time by SHS-SPS. In this regard, the effect produced using W raw powder with different granulometry, and/or the addition of a small amount of graphite prior to the sintering step, on the characteristics of the resulting bulk product is investigated. The influence on mechanical properties and oxidation resistance deriving from the introduction of SiC on the $(Ti_{0.2}Zr_{0.2}Hf_{0.2}Mo_{0.2}W_{0.2})B_2$ matrix is also examined. The obtained results are finally compared with those relative to the SiC free system.

2. Materials and methods

The synthesis of $(Ti_{0.2}Zr_{0.2}Hf_{0.2}Mo_{0.2}W_{0.2})B_2$ by SHS was carried out starting from elemental reactants, namely Hf (Alfa Aesar, cod. 10201,

Table 1

Density, composition, and mechanical properties of the bulk $(Ti_{0.2}Zr_{0.2}Hf_{0.2}Mo_{0.2}W_{0.2})B_2$-based products obtained in this work by SPS from coarser and finer W powders, with no graphite or in presence of 1 wt% of this additive. The corresponding values reported in the literature for the same HEB formulation are also included. BT: Borothermal reduction; BCR: Boro-Carbothermal Reduction; HEBM: High-Energy Ball Milling; LP: Liquid Precursor method; PLS: Pressureless Sintering; RSPS: Reactive SPS; ρ_t= theoretical density of HEB; n.q.: not quantified; n.r.: not reported.

Precursors	Fabrication method	Sintering conditions (T_D, t_d, P)	Secondary phases	ρ (%) (ρ_t, gcm^{-3})	HV (load, N) (GPa)	K_{IC} (MPa m$^{1/2}$)	Reference
HfB_2, ZrB_2, TiB_2, W_2B_5, MoB_2	HEBM-SPS	2000°C/5 min/ 30 MPa	$(Ti_{1.6}W_{2.4})B_4$	n.r.	n.r.	n.r.	[3]
HfO_2, ZrO_2, TiO_2, MoO_3, WO_3, B_4C	BCR-SPS	2000°C/30 min/ 80 MPa	(W,Mo)-rich phase (n.q.)	n.r.	29.4±1.7 (1.96)	n.r.	[18]
Hf, Zr, Ti, Mo, W, B	HEBM-RSPS	Multistep 2000°C/10 min/ 50 MPa	extra B (n.q.)	97.5 (8.56)	26.0±1.5 (1.96)	n.r.	[11]
HfO_2, ZrO_2, TiO_2, MoO_3, WO_3, B	BT-SPS	2000°C/10 min/ 30 MPa	WB	n.r.	27.7±1.1 (1.96)	n.r.	[17]
HfO_2, ZrO_2, TiO_2, MoO_3, WO_3, B_4C, C black	BCR-SPS	2000°C/10 min/ 50 MPa	B_4C+C (2.5 vol%)	96.5 (8.485)	n.r	n.r	[19]
HfO_2, ZrO_2, TiO_2, MoO_3, WO_3, B_4C, C black	BCR-PLS	2100°C/2 h 2200°C/2 h	Multiple phases (W,Mo)B_2 (n.q.)	> 97.7 97.7 (8.40)	n.r n.r	n.r n.r	[21]
H, Zr, Ti, Mo, coarse W, B	SHS-SPS	1950°C/20 min/ 20 MPa	(W,Mo)B_2 (9 wt%), TiO_2 (2 wt%)	96.6±0.7 (8.406)	26.2±1.4 (1)	2.32 ±0.55	**This work**
H, Zr, Ti, Mo, coarse W, B, graphite (1 wt%)	SHS-SPS	1950°C/20 min/ 20 MPa	None	98.6±0.1 (8.406)	26.4±0.7 (1)	2.14 ±0.42	**This work**
H, Zr, Ti, Mo, fine W, B	SHS-SPS	1950°C/20 min/ 20 MPa	(W,Mo)B_2 (<1 wt%), TiO_2 (2 wt%)	96.7±0.6 (8.406)	26.1±0.8 (1)	2.03 ±0.50	**This work**
H, Zr, Ti, Mo, fine W, B, graphite (1 wt%)	SHS-SPS	1950°C/20 min/ 20 MPa	None	98.5±0.7 (8.406)	26.8±0.9 (1)	1.54 ±0.66	**This work**
H, Zr, Ti, Mo, fine W, B, graphite (1 wt%), SiC (20 vol%)	SHS-SPS	1950°C/20 min/ 20 MPa	None*	98.7±0.4 (8.406)	26.5±0.6 (1)	5.11 ±1.11	**This work**

(*) Except for the introduced SiC phase.

99.6 % purity, < 44 μm), Zr (Alfa Aesar, cod 00847, APS 2–3 μm), Ti (Alfa Aesar, cod. 10386, 99 % purity, < 44 μm), Mo (Alfa Aesar, cod. 10030, 99.95 % purity, 3–7 μm), coarse W (Alfa Aesar, cod. 39749, 99.9 % purity, <44 μm) or fine W (Alfa Aesar, cod. 10400, 99.9 % purity, 1–5 μm), and amorphous B (Aldrich, cod 15580, amorphous, ≥ 95 % purity, ≤ 1μm).

Particle size distribution of the two batches of W powders was determined by laser light scattering analysis (CILAS 1180, France). The obtained results are shown in Supplementary Table S1. Whereas metallic elements were used in stoichiometric ratio according to the nominal HEB formulation, an excess of boron (10 mol. %) was employed to balance its further consumption due to borothermal reduction of oxide impurities present on reactants surface, as mentioned in previous studies [22]. Powder mixing was performed using a SPEX 8000 (SPEX CertiPrep, USA) shaker mill device under mild conditions (20 min, BPR=0.2, plastic vials and agata balls). The resulting mixture was then uniaxially cold-pressed to produce cylindrical pellets to be reacted by SHS inside a stainless-steel chamber, first evacuated and then filled with Argon. Reaction activation occurred in few seconds by an electrically heated tungsten filament (R.D. Mathis, USA). The synthesis product was converted in powder form after 1 h ball milling (SPEX CertiPrep, USA, BPR= 2, hardened steel vial and balls) without or in presence of 1 wt% graphite (Sigma-Aldrich, cod 282863, < 20 μm). No traces of iron contamination from milling tools were detected by XRD and SEM/EDS analyses either in the resulting powders or in the corresponding sintered samples. Based on previous ICP-OES (Inductively Coupled Plasma Optical Emission Spectroscopy) measurements carried out in similar systems processed by ball milling at different times and BPR= 2 [33], the maximum level of iron contamination expected in this work is less than 0.1 wt%.

For the preparation of the $(Ti_{0.2}Zr_{0.2}Hf_{0.2}Mo_{0.2}W_{0.2})B_2$-20 vol% SiC composite, the corresponding amount of SiC (Alfa Aesar, cod. 014165, 99.8 % purity) was added to the SHS powders prior to SPS. Particle size distribution of the various mixtures was evaluated by laser light scattering analysis using the device mentioned above. Samples ID used hereafter to indicate the precursors utilized to produce them are: HEB_W_c_0C (coarser W, no graphite, no SiC), HEB_W_c_1C (coarser W, 1 wt%C, no SiC), HEB_W_f_0C (finer W, no graphite, no SiC), HEB_W_f_1C (finer W, 1 wt%C, no SiC), and HEB_W_f_1C_SiC (finer W, 1 wt%C, 20 vol% SiC).

An SPS equipment (515S model, Fuji Electronic Industrial Co., Ltd., Kanagawa, Japan) was employed, under vacuum conditions (about 20 Pa), for powder sintering. About 4.2–4.3 g (SiC-free systems) or 3.7 g (HEB_W_f_1C_SiC) of powders were placed inside cylindrical graphite dies (30 mm external diameter; 15 mm inside diameter; 30 mm height) equipped with two punches (14.7 mm diameter, 20 mm height) through which electric current and mechanical load are applied. Sintering experiments were carried out under temperature-controlled mode using an infrared pyrometer (CHINO, mod. IR-AHS2, Japan) focused on the lateral surface of the die. The SPS conditions adopted to produce the different bulk samples were dwell temperature (T_D), heating rate, holding time, and applied pressure equal to 1950°C, 200 °C/min, 20 min, and 20 MPa. The latter ones were selected according to previous investigations addressed to other quinary HEBs [22,23]. For the sake of reproducibility, each experiment was repeated at least twice.

For characterization purposes, the sintered ceramics were cut, lapped, and polished using progressively finer abrasive paper. Their absolute density was evaluated according to the Archimedes' method using distilled water as immersing medium. The theoretical values of 8.406 g/cm^3 (HEB_W), determined according to the formula used in **Barbarossa et al.** [34], and 7.18 g/cm^3 (HEB_W_f_1C_SiC) were used to calculate the corresponding relative densities. A rule of mixture [35] was utilized to evaluate that of the composite system, using 3.21 g/cm^3 for SiC [36].

Phases identification in SHS and SPS products was performed by X-ray diffraction analysis (rotating anode SmartLab Rigaku, Japan and Philips PW 1830, Netherlands) using Cu Kα radiation, over a range of scattering angles 2ϑ from 20 to 110°, in steps of 0.05° with 15 s acquisition time per angle. Phases content and related microstructural parameters were estimated with the Rietveld method by analyzing the corresponding XRD patterns with the MAUD program [37].

SEM/EDS observations by High Resolution Scanning Electron Microscopy (HRSEM) (mod. S4000, Hitachi, Tokyo, Japan), equipped with a UltraDry EDS Detector (Thermo Fisher Scientific, Waltham, MA, USA), were performed to examine the microstructure and compositional homogeneity of the SHS and SPS samples.

The oxidation behaviour of additive free and SiC containing ceramics was compared by exposing them at high temperatures in air environment using a muffle furnace (LT 24/11/B410, Nabertherm, Lilienthal, Germany). During these tests, specimens were heated at a constant rate (4 °C/min) from room temperature to a maximum level, in the range of 600–1300°C, followed by an isothermal step of 1 h duration. Compositional and microstructural changes of the annealed samples were then examined by XRD and SEM. The linear intercept method or image analysis were used to estimate the average grains size of sintered products from their SEM micrographs,

A Micro Vickers Hardness Testers FUTURE-TECH FM-810 (Kawasaki, Kanagawa 210–0804, Japan) was used to evaluate mechanical properties of SPS samples. To this, the latter ones were embedded into phenolic resin, then lapped and polished. A load of 1 N was applied with a loading time of 15 seconds. The obtained average values were based on at least 5 measurements performed for each sample. Fracture toughness (K_{IC}) was evaluated, using a load of 1 N to make cracks propagate from the indent tips. Crack lengths were determined using a scanning electron microscope (Quanta 400 of Field Electron and Ion Company, Hillsboro, Oregon, US).

The K_{IC} value was then evaluated according to Evans and Charles formula [38,39], namely:

$$K_{IC} = 0.824 \quad P/c^{1.5}$$

where P is the applied load, and c the average crack length measured from the indentation center.

3. Results and discussion

3.1. Processing and microstructural characterization

3.1.1. Effect of W particle size

The preparation by SHS-SPS of $(Ti_{0.2}Zr_{0.2}Hf_{0.2}Mo_{0.2}W_{0.2})B_2$ from its elements was first attempted using relatively coarser W powders, named in this work also as W_c, whose particle size parameters are reported in Supplementary Table S1. From the XRD pattern of the 1 h milled SHS powders shown in Fig. 1(a), it is apparent that the synthesis process did not go to completion, while a multiphase product is obtained. Specifically, as reported in Supplementary Table S2(a), the latter one contained the desired HEB phase, along with several binary and individual metal borides associated to $(Mo_{0.5}Ti_{0.5})B_2$, $(Hf_{0.5}Ti_{0.5})B_2$, $(Ti_{0.5}Zr_{0.5})B_2$, TiB_2, WB_2, WB_4, HfB_2, and ZrB_2. The produced SHS powders were also examined by SEM/EDS. As shown in Supplementary Figure S1(a), they consisted of about 5–15 micrometer-sized aggregates of finer grains. In addition, consistently with XRD analysis, EDS maps confirmed that elemental constituents are not homogeneously distributed across powder particles.

As shown in Fig. 2(a) and Supplementary Table S3(a), the use of W_f powders determined a slight increase in the yield of the HEB phase (from 12 to 17 wt%) (Supplementary Tables S2(a) and S3(a)) and the reduction of the EDS spots size with higher W concentration (Supplementary Figures S1(a)-S1(b)). Nonetheless, the SHS product still consisted of various secondary borides and other phases.

Similar findings were obtained in previous investigation addressed to the fabrication of other HEBs [22,23], to further prove that the SHS reaction dynamic is too fast to allow for the complete diffusion of the
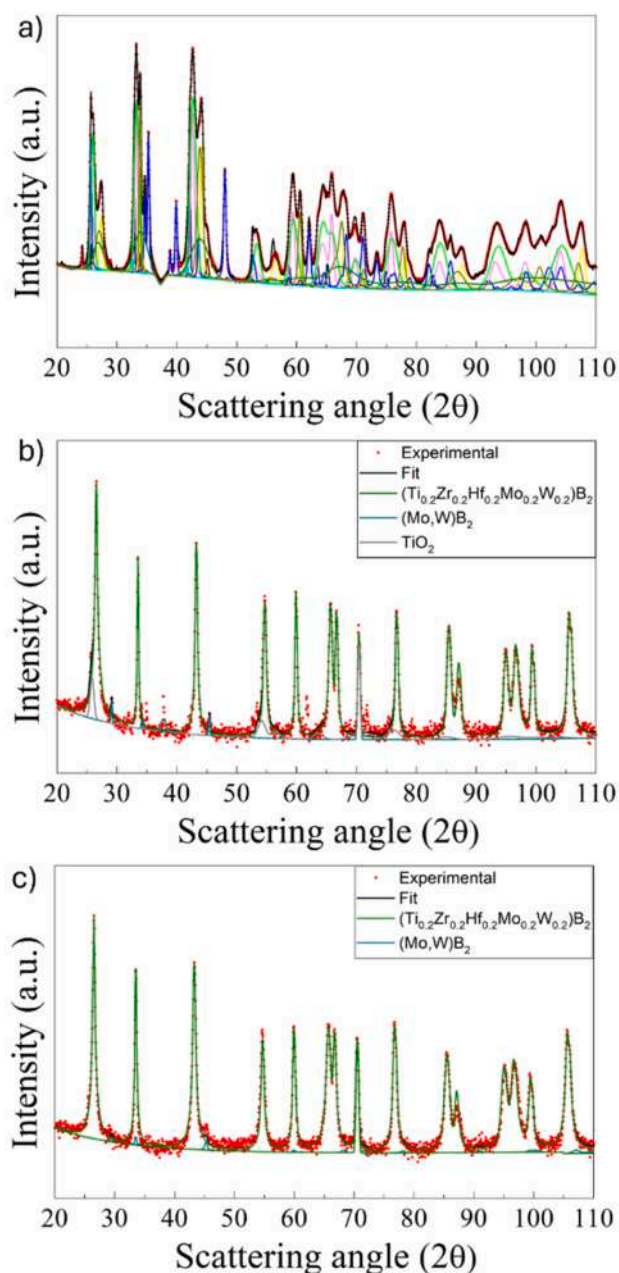
Fig. 1. XRD pattern and related Rietveld refinement of (a) SHS 1 h milled product from coarser W powders and corresponding bulk samples obtained by SPS (b) with no graphite, and (c) with 1 wt%C. (a): (Experimental: red dots; Best Fit: dark solid line; $(Ti_{0.2}Zr_{0.2}Hf_{0.2}Mo_{0.2}W_{0.2})B_2$: olivine solid line; HfB_2 (COD #1510711): navy solid line; $(Ti_{0.5}Zr_{0.5})B_2$ (COD #1510845): magenta solid line; TiB_2 (COD #2002799): yellow solid line; WB_2 (COD #1510852): blue solid line; WB_4 (COD #2310108): wine solid line; ZrB_2 (COD #1510857): light blue solid line; $(Hf_{0.5}Ti_{0.5})B_2$ (COD #1510710): light green solid line; $(Ti_{0.5}Mo_{0.5})B_2$ (COD #1510760): dark yellow solid line). (b)-1(c): Experimental: red dots; Best Fit: dark solid line; $(Ti_{0.2}Zr_{0.2}Hf_{0.2}Mo_{0.2}W_{0.2})B_2$: olivine solid line; $(Mo,W)B_2$ (COD #1510765): cyan solid line; TiO_2 (COD #1010942): violet solid line.

five transition metals across the sample volume and finally form the prescribed quinary solid solution.

Both powder batches were then processed by SPS, under the same conditions (1950°C/20 min/20 MPa). The relative densities of the resulting bulk samples were nearly the same, i.e 96.6±0.7 % (HEB_W_c_0C), and 96.7±0.6 % (HEB_W_f_0C). In contrast, marked

differences were observed from the compositional and microstructural viewpoints. XRD analysis, and related Rietveld refinement of HEB_W_c_0C indicated that a significant enhancement in product composition is achieved during SPS, with an increased HEB content from 12 to 89 wt%. However, about 9 wt% of a secondary boride phase rich in W, also containing Mo, ascribed to $(W,Mo)B_2$, was detected as well (Fig. 1(b) and Supplementary Table S2(b)). The latter outcome was confirmed by SEM/EDS analyses which evidenced the presence of sample regions (circled in Fig. 3(a)) with high W and Mo concentrations, while poorer of the other three metallic elements. More detailed EDS analysis carried out on the black spots observed in Fig. 3(a), whose results are reported in Supplementary Figure S3, evidenced they basically consist of pores filled with oxide impurities.

On the other hand, a significant improvement was obtained in the composition of the SPS product deriving from powders synthesized using W_f precursor. Correspondingly, no secondary phases were detected by XRD analysis and Rietveld refinement (Fig. 2(b) and Supplementary Table S3(b)). Nonetheless, SEM/EDS investigations (Fig. 3 (b)) evidenced that the secondary $(W,Mo)B_2$ phase was not completely eliminated, albeit its content was markedly reduced compared to the HEB_W_c_0C counterpart.

Grain size measurements from SEM micrographs provide the values of 3.78 ± 0.02 and $5.06 \pm 0.06\,\mu m$ for the HEB_W_c_0C and HEB_W_f_0C, respectively.

In summary, it is possible to state that the use of finer W powders highly promotes the formation of the quinary solid solution. Even so, the secondary $(W,Mo)B_2$ phase was still found in the SPS ceramic. In addition to that, SPS samples possessed relative density values below 97 %.

### 3.1.2. Effect of graphite addition

Taking advantage of findings obtained in previous studies focused on other quinary and binary borides [22,23,34], where the addition of small amount of graphite to the SHS powders before their sintering was found highly beneficial, the effect of the introduction of 1 wt% of this additive prior to SPS on the characteristics of the resulting ceramics was also examined in this work.

First, an increase of samples densification from 96.6-96.7% to 98.5-98.6% was achieved during SPS either when starting from finer or coarser W precursors. As explained in detail elsewhere [22], this is because graphite plays a key role for the carbothermal reduction of oxides impurities present in the processing powders, so that their sinterability is enhanced, but it also exerts a lubricating action to further facilitate sample consolidation.

The effect produced on product composition can be deduced from the XRD analysis results reported in Fig. 1(c) - Supplementary Table S2 (c) and Fig. 2(c) - Supplementary Table S3(c), for the case of HEB_W_c_1C and HEB_W_f_1C systems, respectively. As for the product deriving from coarser W powders, the introduction of graphite led to a marked reduction of the amount of the secondary $(W,Mo)B_2$ phase, from 9 wt% (Section 3.1.1) to less than 1 wt%. This outcome was confirmed when examining the corresponding SEM micrograph and related EDS maps shown in Fig. 3(c). The removal of oxide layers surrounding particles, caused by the introduction of graphite, apparently facilitates the diffusion of metallic constituents across the sample to form the prescribed HEB phase.

The XRD analysis carried out on samples prepared from finer W confirmed the obtainment of a single-phase solid solution (Fig. 2(c)- Supplementary Table S3(c)). Furthermore, SEM/EDS observations (Fig. 3(d)) testify that graphite introduction allowed for the elimination of the W-rich regions locally observed in the ceramics produced without using such additive (Fig. 3(b)). Consequently, it is proved, once more, that graphite plays a valuable contribution for the synthesis of the homogeneous multicomponent diboride phase.

It should be pointed out that the lattice parameter values for the obtained HEB phase, i.e. a= 3.0852–3.0889 Å, and c=3.3533–3.3582 Å (Table S3), are in line with those reported in previous works, where the
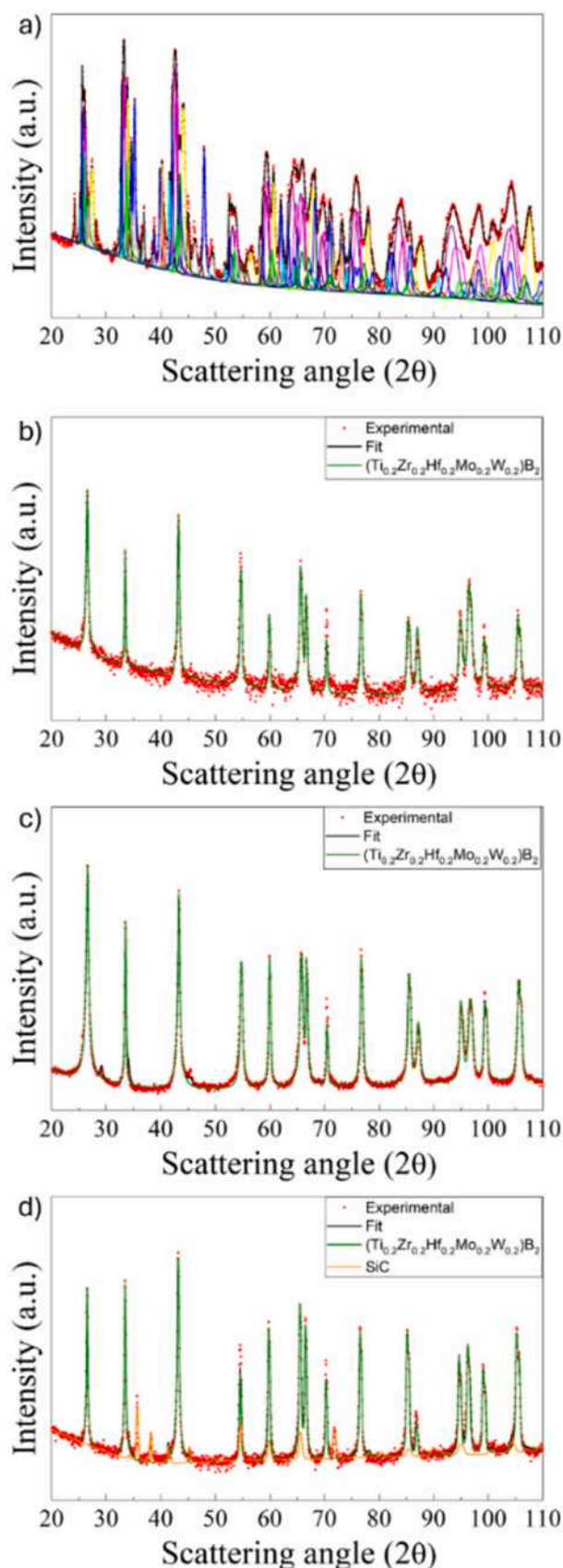
Fig. 2. XRD pattern and related Rietveld refinement of (a) SHS 1 h milled product from finer W powders and corresponding bulk samples obtained by SPS (b) with no graphite, (c) with 1 wt%C, (d) with 1 wt%C and 20 vol%SiC. (a): (Experimental: red dots; Best Fit: dark solid line; $(Ti_{0.2}Zr_{0.2}Hf_{0.2}Mo_{0.2}W_{0.2})B_2$: olivine solid line; $(Hf_{0.5}Zr_{0.5})B_2$ (PCD #1932158): purple solid line; HfB_2 (COD #1510711): navy solid line; $(Ti_{0.5}Zr_{0.5})B_2$ (COD #1510845): magenta solid line; TiB_2 (COD #2002799): yellow solid line; WB_2 (COD #1510852): blue solid line; WB_4 (COD #2310108): wine solid line; ZrB (COD #1510857): light blue solid line; Mo (COD #4001308): pink solid line; $Mo_2B_{0.4026}$ (COD #1511521):light grey solid line; MoO_2 (COD #1548687):dark grey solid line; $Mo_{0.875}Zr_{125}$ (COD #1522701): light orange solid line; $(Hf_{0.5}Ti_{0.5})B_2$ (COD #1510710): light green solid line). (b)-2(d): (Experimental: red dots; Best Fit: dark solid line; $(Ti_{0.2}Zr_{0.2}Hf_{0.2}Mo_{0.2}W_{0.2})B_2$: olivine solid line; SiC (COD # 9010158): orange solid line).

(caption on next column)

synthesis of the same system succeeded, i.e. a=3.0790 Å, c=3.3389 Å [11] and a=3.0823 Å, c=3.3446 Å [19].

Relatively coarser grains, compared to the systems considered in Section 3.1.1, were found in the SPS samples produced when graphite was added, with the measured values equal to 11.30 ± 0.30 and 13.40 ± 0.53 μm for the HEB_W_c_1C and HEB_f_1C, respectively. This fact could be associated to the corresponding reduction of disperse oxides particles, whose presence represents an obstacle to the movement of grain boundaries.

3.1.3. Bulk $(Ti_{0.2}Zr_{0.2}Hf_{0.2}Mo_{0.2}W_{0.2})B_2$-SiC composite

Based on the results described in Section 3.1.2, the precursors used for the HEB_W_f_1C system (fine W precursor, 1 wt% graphite) are also considered for the preparation of the SiC containing HEB composite samples. The SPS conditions were also the same adopted for the additive-free systems, i.e. 1950°C/20 min/20 MPa.

The first benefit produced using SiC was to make powder consolidation easier. Indeed, as shown in Supplementary Figure S2, where sample shrinkage during SPS of the HEB_W_f_1C-SiC system is compared to that of the monolithic diboride, it is proven that SiC promotes powders densification. This effect is particularly evident during the non-isothermal step (inset of Figure S2).

The two shrinkage curves almost overlap for about 5.4 min from the current application, during which no variation in this parameter was recorded for both mixtures, except for a slight increase (0.1 mm) observed after about 4 min, likely due to particles rearrangement. However, when the temperature approached 1100°C, the shrinkage of the SiC containing sample increased, whereas no changes were manifested by its additive free counterpart, until T equals about 1250°C (6.3 min). This effect tends to vanish progressively due to the high temperature conditions required to make the formation of the $(Ti_{0.2}Zr_{0.2}Hf_{0.2}Mo_{0.2}W_{0.2})B_2$ phase possible. Finally, the shrinkage values recorded at the end of the isothermal step (t=30 min) were about 1.73 and 1.87 mm for the HEB and HEB-SiC systems, respectively. The relative density of resulting composite samples was 98.7±0.4 %. As for product composition, the first issue to be checked was if the addition of SiC hindered, in some way, the transformation of secondary phases present in SHS powders (Fig. 2(a) - Supplementary Table S3(a)) into the high-entropy phase. XRD analysis associated to the Rietveld refinement (Fig. 2(d)-Supplementary Table S4) testifies that no other phases, in addition to the expected ones (HEB and SiC), were detected. Also, the relative SiC content, as estimated by this analysis (7 wt%, equivalent to about 21.5 vol%), was rather close to the amount initially added to SHS powders.

SEM micrographs and corresponding EDS maps shown in Fig. 4 provided further evidence of the obtainment of a highly dense composite material, consisting of $(Ti_{0.2}Zr_{0.2}Hf_{0.2}Mo_{0.2}W_{0.2})B_2$ as a matrix, characterized by a very uniform concentration of the five metallic constituents, with SiC particles evenly distributed across the sample.

The measured grain size of HEB-SiC samples from the related SEM micrographs equal to 8.37 ± 2.90, i.e. lower than the value (13.40 ±
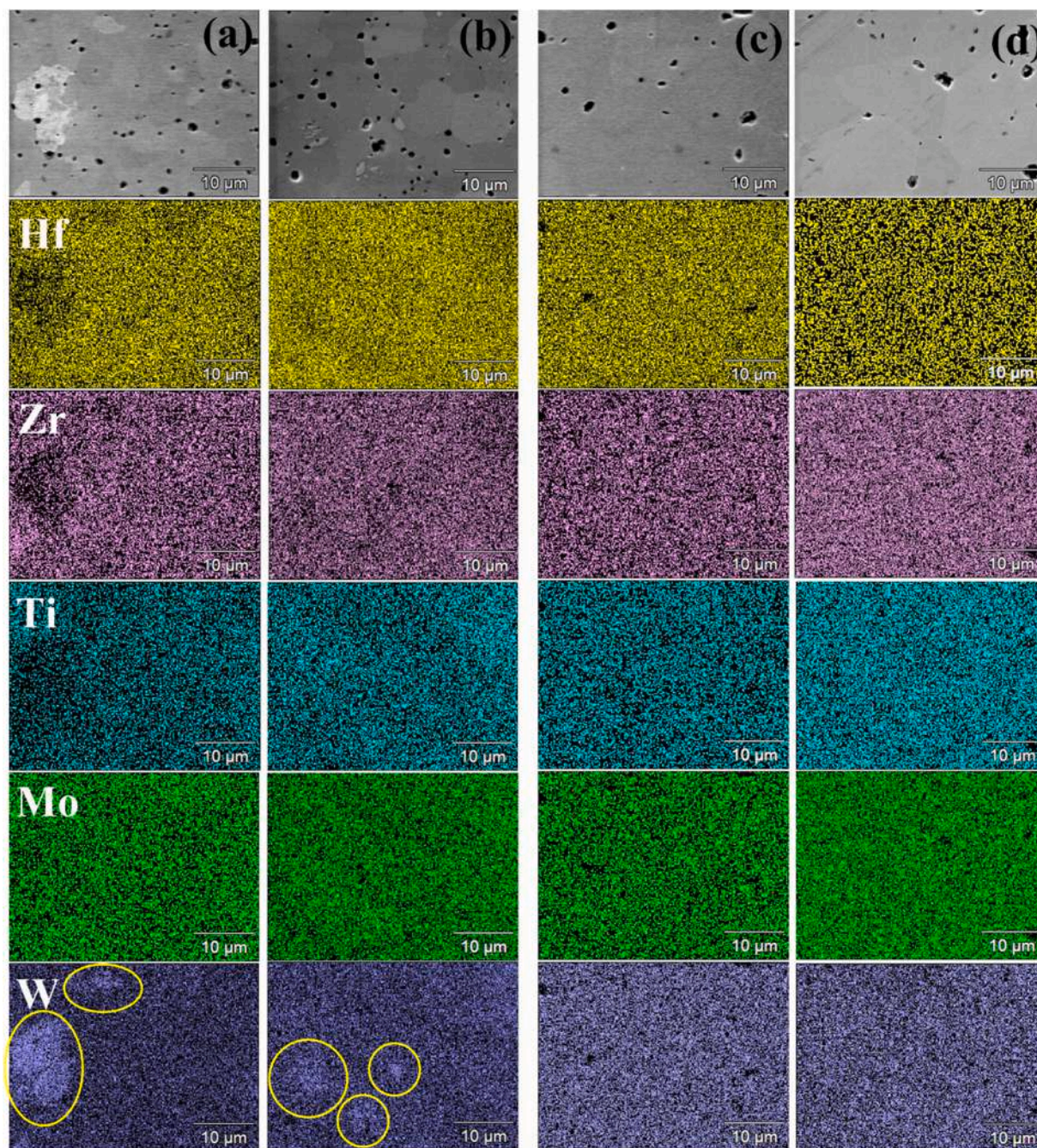
Fig. 3. Cross sectional SEM micrographs and related EDS elemental maps of $(Ti_{0.2}Zr_{0.2}Hf_{0.2}Mo_{0.2}W_{0.2})B_2$ samples obtained by SPS from SHS powder with no graphite addition: (a) coarser, (b) finer W powders, and with 1 wt% graphite addition: (c) coarser, and (d) finer W powders.

0.53 μm) measured when considering the SiC-free sample using the same W powder with 1 wt% graphite. Thus, the presence of SiC apparently inhibits grains growth of the HEB ceramic.

Based on the study above, it is possible to state that the addition of silicon carbide does not determine undesired reactions with any of the several phases present in SHS powders, so that the predicted two constituents are the only ones present in the sintered ceramic.

3.2. Oxidation behaviour

The oxidation resistance of HEB_W_f_1C and HEB_W_f_1C-SiC samples was deduced on the basis of weight, compositional, and microstructural changes they manifested when exposed for 1 h to air heat treatment in a furnace at different temperatures, in the range 600–1300°C.

Supplementary Figure S4(a) shows the color variation, with respect to the initial grey-brown, of SiC-free samples as the oxidation temperature became progressively more severe. Major changes can be observed at 800°C or higher temperatures, with the surface of the treated ceramics that turns first to light blue then to yellow-orange. In addition, after their annealing at 1200°C and 1300°C, samples displayed a very irregular surface, some cracks appeared, to indicate their advanced degradation. Apparently, a different behavior was manifested by HEB_W_f_1C-SiC specimens, with lower changes observed up to 1000°C, while their surface became rough, but no cracks were formed, at 1200°C (Figure S4 (b)).

The discrepancies above between the two systems are even more evident when their weight changes after the oxidation treatment are
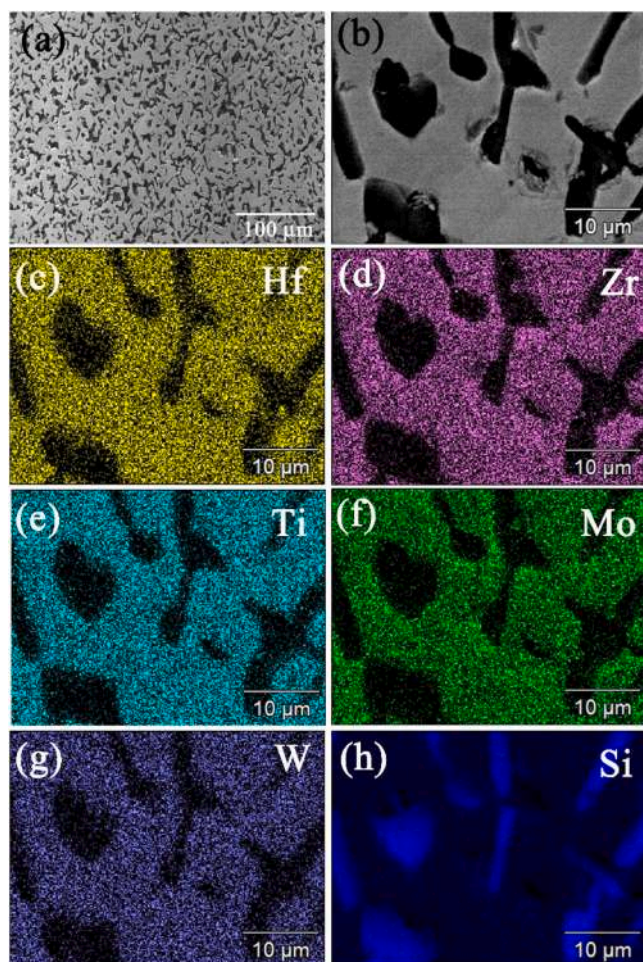
Fig. 4. Cross sectional SEM micrographs and related EDS elemental maps of $(Ti_{0.2}Zr_{0.2}Hf_{0.2}Mo_{0.2}W_{0.2})B_2$-SiC sample obtained by SPS: (a) general, (b) detailed views, and (c)-(h) related EDS elemental maps.

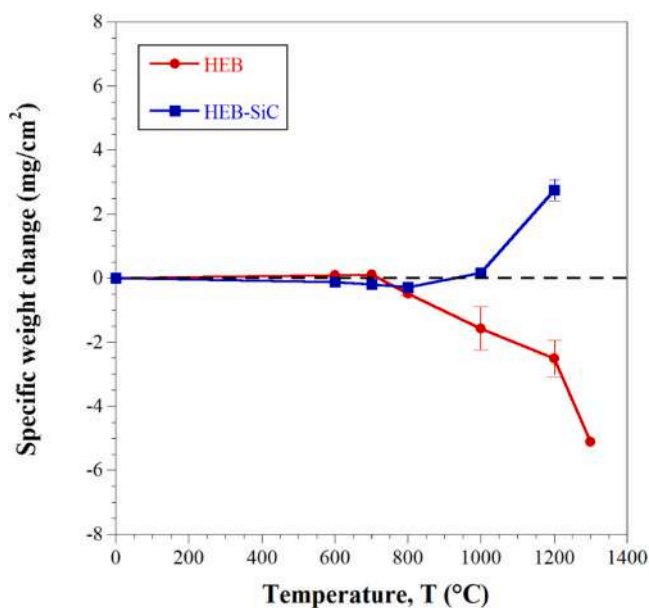**Fig. 5.** Comparison of weight changes per surface area of additive free and SiC containing $(Ti_{0.2}Zr_{0.2}Hf_{0.2}Mo_{0.2}W_{0.2})B_2$ samples during oxidation tests carried out in air furnace as a function of temperature (t=1 h).

compared in Fig. 5. Both ceramics display only slight changes up to 700°C. However, as the temperature was raised at 800°C or higher levels, additive free samples lose progressively their mass. In contrast, only minor weight variations occur up to 1000°C in the composite ceramics, while a mass gain was recorded at 1200°C. These findings are consistent with those ones recently observed by Pakhomova et al. [8], when the oxidation behavior SiC containing $(Ti_{0.2}Hf_{0.2}Nb_{0.2}Ta_{0.2}Mo_{0.2})$ B_2, and $(Ti_{0.2}Zr_{0.2}Hf_{0.2}Ta_{0.2}Mo_{0.2})B_2$ ceramics was compared with the monolithic counterparts.

In addition to the outcomes discussed above, the analysis of compositional and microstructural evolution is essential to define samples behavior during oxidation tests. Based on XRD patterns shown in Figs. 6(a)-6(b), no additional phases were detected in HEB_W_f_1C and HEB_W_f_1C-SiC systems up to 600°C. On the other hand, when the temperature was increased to 700°C, XRD peaks of metal oxides (namely, WO_3, TiO_2, and ZrO_2) were found on the surface of both ceramics, even if HEB still resulted to be the dominant phase. A different situation was encountered at 800°C. Correspondingly, the additive-free system (Fig. 6(a)) was basically almost completely covered by the oxides found at 700°C, with the diboride phase barely detected by this analysis. In contrast, when considering the SiC-containing counterpart (Fig. 6(b)), the HEB peaks intensity is still very high, compared to those of HfO_2, TiO_2, and ZrO_2, while no WO_3 was found. However, as the temperatures of the oxidation treatment was augmented to 1000°C, only HfO_2, TiO_2, and ZrO_2 phases were detected by XRD. A further increase of the temperature to 1200°C led to the formation of mixed oxides like $ZrTiO_2$ on the surface of both ceramics. In addition, some silicate phases, either crystalline, such as $ZrSiO_4$ and $HfSiO_4$, detected by XRD (Fig. 6(b)) or amorphous, were also formed on the HEB-SiC system.

More direct evidence of the behavior exhibited by the two ceramics during the oxidation test is provided by SEM observations, whose results are shown in Figs. 7(a)-7(d). Let us first examine the sample with no SiC (Figs. 7(a)-7(c)). When the latter was heat treated at 800°C, an oxide layer, with thickness of about 15–20 μm, was produced on the sample surface (Fig. 7(a)). This layer is very poor of Mo, but also W deficient, particularly on the more external sample side. The high volatility of the oxides formed by these two elements (WO_3 and MoO_3), which are allowed to leave the material, readily explains the latter feature [40]. As the temperature was raised to 1000°C, the thickness of the oxide layer became nearly twice (35–40 μm) (Fig. 7(b)). Moreover, this layer could be considered divided in two portions with different characteristics. The external one is very porous, deficient in both Mo and W, while rich of the other metallic elements, particularly Ti. The second portion, placed on the inner sample side, is more compact, still poor in Mo, whereas W content is comparable to that of the bulk, not oxidized, ceramic. This is consistent with the XRD analysis results discussed above, where the presence of WO_3 on the samples surface was detected up to 1000°C, whereas there was no clear evidence of the presence of MoO_3. This behavior can be readily justified by considering the data reported in Supplementary Figure S5, where vapor pressure of tungsten and molybdenum trioxides is reported as a function of temperature. It can be clearly seen that MoO_3 shows higher volatility compared to WO_3. This turns out into a higher evaporation rate of MoO_3 which explains the lower content of the latter in the oxide layer (cf. Fig. 6 and Fig. 7).

Fig. 7(c) shows that, when the sample was annealed at 1200°C, the outer layer was found separated from the inner one, which became less compact than the oxide product observed at 1000°C. Each of them became approximately 50 μm thick, while both maintained the compositional characteristics of the sample heat treated at 1000°C. The marked sample degradation observed under the latter condition is perfectly consistent with the significant weight loss correspondingly recorded (Fig. 5).

SEM/EDS analysis outcomes provided the direct evidence that the introduction of the SiC additive was highly beneficial for the protection of the HEB matrix from the oxidazing environment. This can be clearly deduced from Fig. 7(d), where a SEM micrograph and related EDS maps
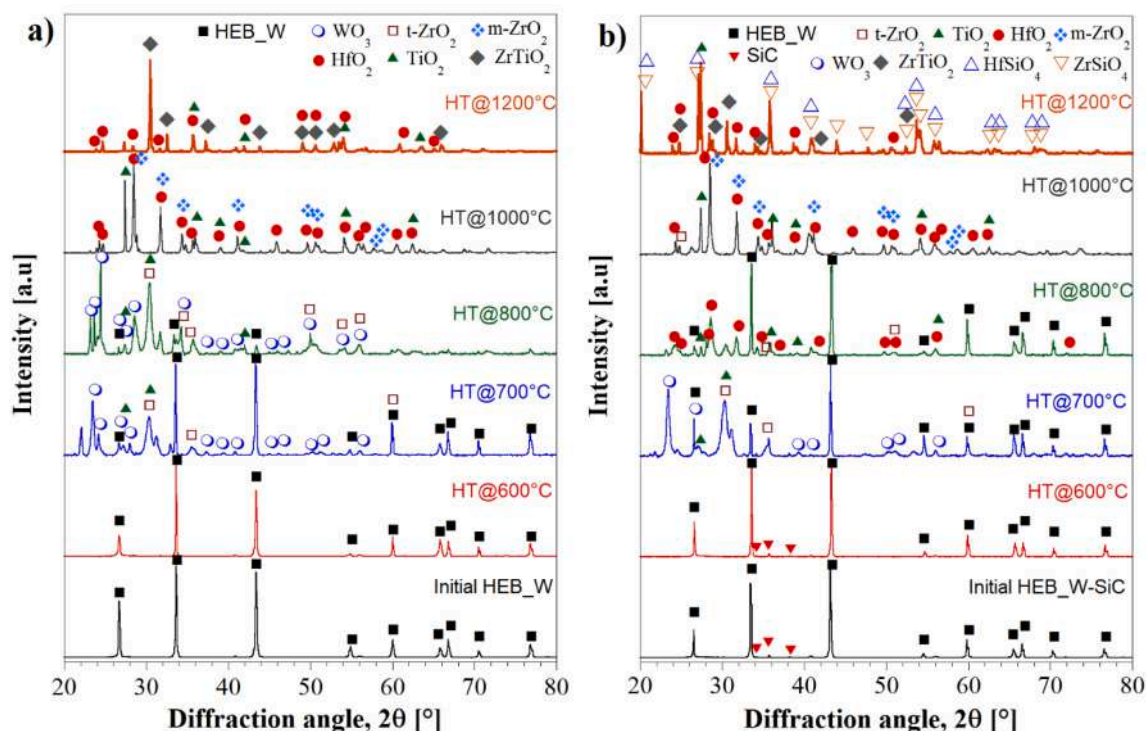
Fig. 6. XRD patterns of HEB_W (a) and HEB_W–SiC (b) samples after being heat treated in air furnace at different temperatures.

of the HEB_W_f_1C-SiC sample heat treated at 1200°C are reported. The general situation appears immediately to be much better than the dramatic one shown in Fig. 7(c) for the additive free ceramic oxidized under the same condition. An external oxide layer, with thickness of about 40–50 μm, a very low Mo content, also W deficient, and particularly rich in Ti, was produced. Silicon appears to be quite uniformly distributed in the layer, likely involved in the formation of crystalline silicates like $ZrSiO_4$ and $HfSiO_4$, identified by XRD (Fig. 6(b)), and other amorphous phases. Interestingly, another layer, about 15–20 μm thick, is encountered when moving toward the bulk of the sample. Such oxidized inner layer is very rich in Mo and W, relatively poorer in the other transition metals, while Si seems to be uniformly distributed on it. It is then presumable that such layer consists of Mo- and W-rich silicates (or borosilicates) which are responsible for the protection of the material from the oxidation.

The understanding of the oxidation mechanisms of the HEB here investigated and the role played in this regard by SiC involve both thermodynamic and kinetic considerations. In fact, oxidation of metal diborides involves several phenomena such as surface reaction, oxygen diffusion through porous oxide scale and liquid boria, as well as permeation and evaporation of the latter. Parthasarathy et al. [41] and, more recently, Mogilevsky and Cinibulk [42] provided, for the case of individual metal borides-based systems, an excellent schematization of the latter phenomena, as well as a mathematical model to describe them. However, when considering HEBs, the oxidation mechanism is made further complicated by the formation of several multicomponent phases, as confirmed in the present study by the various individual and mixed oxides detected by XRD analysis on the surface of the oxidized samples (Fig. 6). Overall, the identification of the detailed oxidation mechanism of this quinary system clearly requires a thorough experimental and theoretical investigation, which is beyond the scope of the present work and deserves a dedicated study. In this regard, to provide a reliable oxidation mechanism for such complex systems, the behavior of simpler multicomponent borides (binary and ternary), involving the same transition metals should be first considered. This approach will permit, taking also advantage of the information available in the literature for individual diboride systems, to the understanding of the related mechanism.

Although further studies are needed to draw definitive conclusions, based on the outcomes described above, it is possible to state that the presence of SiC clearly hinders the progressive loss of volatile Mo and W oxides, so that the degradation rate of the HEB phase under investigation was markedly lowered.

3.3. Mechanical properties

Vickers hardness, and fracture toughness values of the different samples obtained in this work are shown in Table 1. It should be noted that no fracture toughness data of additive free $(Ti_{0.2}Zr_{0.2}Hf_{0.2}Mo_{0.2}W_{0.2})B_2$ are available so far in literature.

No particular effect was displayed by the use of finer W and/or the addition of graphite on the Vickers hardness of samples fabricated in this work, with HV values in the range of 26.1–26.8 GPa. The latter values were in line with results (26 GPa) reported by **Qin et al.** [11], where the HEB ceramic was produced by Reactive SPS from elemental powders preliminarily activated by HEBM. Superior hardness properties were obtained by Gild et al. [18] and Zhang et al. [17], i.e. 29.4 and 27.7 GPa, respectively, but the secondary phases present in the corresponding sintered samples (Table 1) are expected to affect the measured values.

Table 1 also indicates that the SiC free samples possessed very low fracture toughness values, i.e. 2.32 MPa $m^{0.5}$ at most. Moreover, the introduction of graphite prior to SPS made the resulting K_{IC} worser. This can be explained by the fact that the oxides impurities present in ceramics produced with no graphite hinder the propagation of the cracks formed by Vickers indentation (Figure S6(a)). On the other hand, the reduction of such oxides makes their propagation easier (Figure S6(b)), so that the resulting K_{IC} is correspondingly lowered. Because of their stress concentration effect, oxide particles act as crack tip attractors, deviating the crack path from its normal straight direction. In this way, the fracture surface is increased and the K_{IC} value as well.

The introduction of SiC to the HEB matrix provided a marked improvement on the K_{IC} value, which increased up to 5.11 MPa $m^{0.5}$
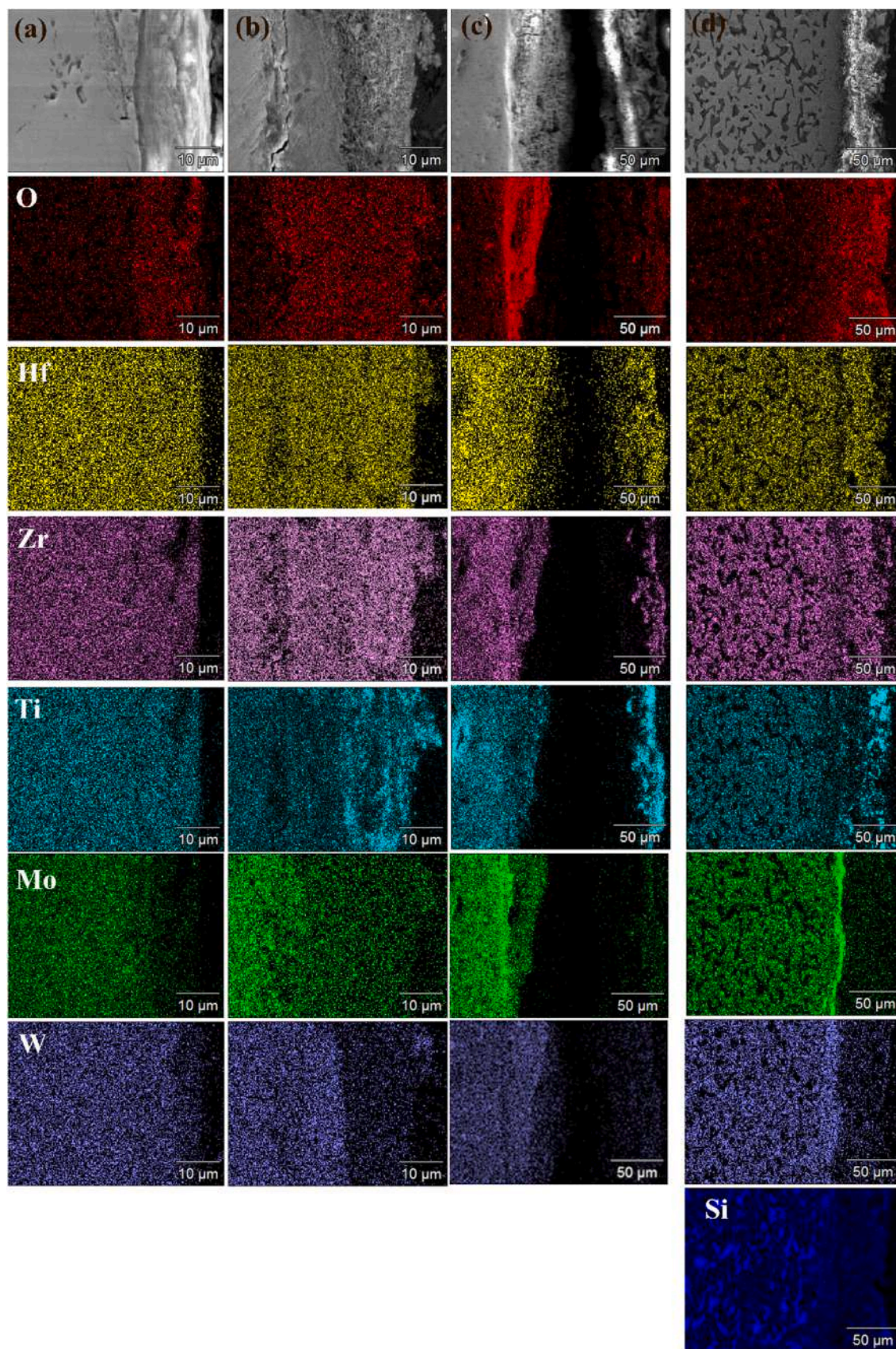
Fig. 7. Cross sectional SEM micrographs and related EDS elemental maps of SiC free samples after oxidation at (a) 800°C, (b) 1000°C, (c) 1200°C, and (d) $(Ti_{0.2}Zr_{0.2}Hf_{0.2}Mo_{0.2}W_{0.2})B_2$ -SiC product heat treated in air furnace at 1200°C.

(Table 1). This is strictly correlated to the deflection and branching phenomena occurring when, during their propagation, cracks encounter the carbide phase disperse into the composite sample (Figure S6(c)).

4. Conclusions

The difficult target of synthesizing the $(Ti_{0.2}Zr_{0.2}Hf_{0.2}Mo_{0.2}W_{0.2})B_2$ ceramic as a single phase is achieved in this work by combining the SHS and SPS methods. To this aim, the use of relatively fine W precursors and the addition of a small amount of graphite to the SHS powders provide a synergic contribution for the abatement of kinetic limitations present during the synthesis of such high entropy boride, which generally leads to the formation of W-rich secondary phases. The approximately 98.5 % dense and homogeneous product obtained by SPS shows Vickers hardness of about 26.8 GPa, whereas fracture toughness and oxidation resistance at high temperature properties are both very modest. The latter criticisms can be overcome with the introduction of 20 vol%SiC. Correspondingly, a marked improvement of the K_{IC} value from 2.32 (at most, for the additive free system) to 5.11 MPa m$^{1/2}$ (composite sample) is obtained. Moreover, this additive is found to markedly improve the scarce resistance of the $(Ti_{0.2}Zr_{0.2}Hf_{0.2}Mo_{0.2}W_{0.2})B_2$ material when exposed to oxidative environments, which is primarily caused by the volatilization of Mo- and W-oxides. In the composite ceramic, the latter phenomenon can be significantly lowered by the formation of silicate phases, which incorporates such volatile oxides, and consequently leads to a reduced degradation rate.

Generally speaking, it should be mentioned that the addition of SiC reduces the intrinsic refractory nature of the UHTCs, so that their performances at temperatures exceeding 1600°C might be negatively affected. Nonetheless, when considering the $(Ti_{0.2}Zr_{0.2}Hf_{0.2}Mo_{0.2}W_{0.2})B_2$ system investigated in this work, the detrimental volatilization of W- and Mo- oxides occurs at 800°C, i.e. well below 1600°C, so that the use of SiC provide a beneficial improvement of its resistance in a wider temperature range.

CRediT authorship contribution statement

Simone Barbarossa: Writing – review & editing, Methodology, Investigation, Data curation. **Mariano Casu:** Writing – review & editing, Validation, Methodology, Investigation, Data curation. **Roberto Orrù:** Writing – review & editing, Writing – original draft, Validation, Supervision, Resources, Methodology, Investigation, Funding acquisition, Conceptualization. **Paolo Ferro:** Writing – review & editing, Validation, Methodology, Investigation. **Sebastiano Garroni:** Writing – review & editing, Validation, Supervision, Methodology, Investigation, Data curation. **Laura Caggiu:** Methodology, Investigation. **Costantino Cau:** Methodology, Investigation. **Giacomo Cao:** Writing – review & editing, Supervision, Investigation, Funding acquisition. **Antonio Mario Locci:** Writing – review & editing, Supervision, Methodology, Investigation, Data curation.

Declaration of Competing Interest

The authors declare the following financial interests/personal relationships which may be considered as potential competing interests: Roberto Orru' reports financial support was provided by Italian Ministry for Research and Education (MUR). Giacomo Cao reports financial support was provided by Italian Ministry for Research and Education (MUR). If there are other authors, they declare that they have no known competing financial interests or personal relationships that could have appeared to influence the work reported in this paper.

Data availability

The authors do not have permission to share data.

Appendix A. Supporting information

Supplementary data associated with this article can be found in the online version at doi:10.1016/j.jallcom.2024.176492.

References

[1] L. Feng, W.G. Fahrenholtz, D.W. Brenner, Annu Rev. Mater. Res 51 (2021) 165–185, https://doi.org/10.1146/annurev-matsci-080819-121217.
[2] F. Wang, F. Monteverde, B. Cui, Int. J. Extrem. Manuf. 5 (2) (2023) 022002, https://doi.org/10.1088/2631-7990/acbd6e.
[3] J. Gild, Y. Zhang, T. Harrington, S. Jiang, T. Hu, M.C. Quinn, W.M. Mellor, N. Zhou, K. Vecchio, J. Luo, Sci. Rep. 6 (2016) 37946, https://doi.org/10.1038/srep37946.
[4] S.R. Levine, E.J. Opila, M.C. Halbig, J.D. Kiser, M. Singh, J.A. Salem, J. Eur. Ceram. Soc. 22 (14-15) (2002) 2757–2767, https://doi.org/10.1016/S0955-2219(02)00140-1.
[5] L. Silvestroni, D. Sciti, L. Zoli, A. Balbo, F. Zanotto, R. Orrù, R. Licheri, C. Musa, L. Mercatelli, E. Sani, Renew. Energy 133 (2019) 1257–1267, https://doi.org/10.1016/j.renene.2018.08.036.
[6] S. Barbarossa, R. Orrù, G. Cao, A. Balbo, F. Zanotto, E. Sani, J. Alloy. Compd. 935 (2023) 167965, https://doi.org/10.1016/j.jallcom.2022.167965.
[7] G. Tallarita, R. Licheri, S. Garroni, S. Barbarossa, R. Orrù, G. Cao, J. Eur. Ceram. Soc. 40 (2020) 942–952, https://doi.org/10.1016/j.jeurceramsoc.2019.10.031.
[8] E. Pakhomova, G. Cao, R. Orrù, S. Garroni, P. Ferro, R. Licheri, Materials 17 (2024) 718, https://doi.org/10.3390/ma17030718.
[9] W. Yang, G. Xiao, Z. Ren, Scr. Mater. 227 (2023) 1152992023, https://doi.org/10.1016/j.scriptamat.2023.115299.
[10] Z.-J. Huang, J.-P. Chen, Y. Tian, L. Xu, W.-M. Guo, H.-T. Lin, J. Eur. Ceram. Soc. 44 (8) (2024) 5211–5215, https://doi.org/10.1016/j.jeurceramsoc.2024.02.050.
[11] M. Qin, J. Gild, H. Wang, T. Harrington, K.S. Vecchio, J. Luo, J. Eur. Ceram. Soc. 40 (12) (2020) 4348–4353, https://doi.org/10.1016/j.jeurceramsoc.2020.03.063.
[12] X. Zhang, W. Li, H. Tian, J. Liu, C. Li, H. Dong, J. Chen, M. Song, B. Chen, H. Sheng, S. Wang, D. Zhang, H. Zhang, J. Phys. Chem. Lett. 12 (12) (2021) 3106–3113, https://doi.org/10.1021/acs.jpclett.1c00399.
[13] R. Mitra, T. Maity, N. Sharma, T. Tiwari, T. Maiti, K. Biswas, J. Mater. Res 38 (8) (2023) 2122–2136, https://doi.org/10.1557/s43578-023-00956-4.
[14] S. Ye, J. Zhu, P. L, M. Li, N. Yan, H. Wang, Mater. Today Commun. 34 (2023) 105228, https://doi.org/10.1016/j.mtcomm.2022.105228.
[15] R.-F. Guo, H.-R. Mao, P. Shen, J. Eur. Ceram. Soc. 43 (14) (2024) 5763–5773, https://doi.org/10.1016/j.jeurceramsoc.2023.05.042.
[16] Q. Zou, H. Gu, Y. Li, Z. Li, P. Liang, Y. Luo, J. Am. Ceram. Soc. 106 (5) (2023) 2764–2772, https://doi.org/10.1111/jace.18967.
[17] Y. Zhang, S.-K. Sun, W. Zhang, Y. You, W.-M. Guo, Z.-W. Chen, J.-H. Yuan, H.-T. Lin, Ceram. Int. 46 (9) (2020) 14299–14303, https://doi.org/10.1016/j.ceramint.2020.02.214.
[18] J. Gild, A. Wright, K. Quiambao-Tomko, Md.S. bin Hoque, J.L. Braun, B. Bloomfield, D. Martinez, T. Harrington, K.S. Vecchio, P.E. Hopkins, J. Luo, Ceram. Int. 46 (5) (2020) 6906–6913, https://doi.org/10.1016/j.ceramint.2019.11.186.
[19] F. Monteverde, F. Saraga, M. Gaboardi, L. Feng, G. Hilmas, W. Fahrenholtz, J. Am. Ceram. Soc. 105 (11) (2022) 6910–6923, https://doi.org/10.1111/jace.18619.

[20] M. Gaboardi, F. Monteverde, F. Saraga, G. Aquilanti, L. Feng, W. Fahrenholtz, G. Hilmas, Acta Mater. 239 (2022) 118294, https://doi.org/10.1016/j.actamat.2022.118294.

[21] S.M. Smith, W.G. Fahrenholtz, G.E. Hilmas, J. Eur. Ceram. Soc. 43 (12) (2023) 5168–5173, https://doi.org/10.1016/j.jeurceramsoc.2023.04.050.

[22] S. Barbarossa, R. Orrù, S. Garroni, R. Licheri, G. Cao, Ceram. Int. 47 (2021) 6220–6231, https://doi.org/10.1016/j.ceramint.2020.10.200.

[23] S. Barbarossa, R. Orrù, V. Cannillo, A. Iacomini, S. Garroni, M. Murgia, G. Cao, Ceramics 4 (2021) 108–120, https://doi.org/10.3390/ceramics4020010.

[24] W. Gong, T. Wang, W. Luo, Y. Du, L. Ye, R. Song, H. Cui, T. Zhao, W. Yang, Z. Dai, Y. Hong, Materials 16 (2023) 7431, https://doi.org/10.3390/ma16237431.

[25] Guo R., L, Z, Li L, Liu Y, Zheng R, Ma C,. J. Eur. Ceram. Soc. 2022,42(5): 2127–2134. https://doi.org/10.1016/j.jeurceramsoc.2021.12.036.

[26] A.C. Murchie, J.L. Watts, W.G. Fahrenholtz, G.E. Hilmas, J. Int, Appl. Ceram. 19 (4) (2022) 2293–2299, https://doi.org/10.1111/ijac.14026.

[27] Y. Zhang, Z.B. Jiang, S.K. Sun, W.M. Guo, Q.S. Chen, J.X. Qiu, K. Plucknett, H.T. Lin, J. Eur. Ceram. Soc. 39 (13) (2019) 3920–3924, https://doi.org/10.1016/j.jeurceramsoc.2019.05.017.

[28] X.Q. Shen, J.X. Liu, F. Li, G.J. Zhang, Ceram. Int. 45 (18) (2019) 24508–24514, https://doi.org/10.1016/j.ceramint.2019.08.178.

[29] J.X. Liu, X.Q. Shen, Y. Wu, F. Li, Y. Liang, G.J. Zhang, J. Adv. Ceram. 9 (4) (2020) 503–510, https://doi.org/10.1007/s40145-020-0383-8.

[30] Y. Zhang, S.K. Sun, W.M. Guo, L. Xu, W. Zhang, H.T. Lin, J. Adv. Ceram. 10 (1) (2021) 173–180, https://doi.org/10.1007/s40145-020-0418-1.

[31] Y. Gong, Z. Yang, X. Wei, S. Song, S. Ma, J. Mater. Sci. 57 (20) (2022) 9218–9230, https://doi.org/10.1007/s10853-022-07238-0.

[32] Y.Y. Cheng, L. Zhou, J.X. Liu, Y.F. Tan, G.J. Zhang, J. Am. Ceram. Soc. 106 (8) (2023) 4997–5004, https://doi.org/10.1111/jace.19128.

[33] C. Musa, R. Licheri, R. Orrù, G. Cao, D. Sciti, L. Silvestroni, L. Zoli, A. Balbo, L. Mercatelli, M. Meucci, E. Sani, Materials 9 (6) (2016) 489, https://doi.org/10.3390/ma9060489.

[34] S. Barbarossa, M. Casu, R. Orrù, A.M. Locci, G. Cao, S. Garroni, D. Bellucci, V. Cannillo, Ceram. Int. 50 (7) (2024) 12158–12166, https://doi.org/10.1016/j.ceramint.2024.01.119.

[35] Matthews, F.L.; Rawlings, R. Composite Materials: Engineering and Science, firsst ed. Woodhead Publishing, Sawston, UK, 1999; 1–480.

[36] J.F. Shackleford, W. AlexanderCRC Material Science and Engineering Handbook, third ed., CRC Press2001.

[37] L. Lutterotti, R. Ceccato, R. Dal Maschio, E. Pagani, Mater. Sci. Forum 87 (1998) 278–281, https://doi.org/10.4028/www.scientific.net/msf.278-281.87.

[38] C.B. Ponton, R.D. Rawlings, Mater. Sci. Technol. 5 (1989) 865–872, https://doi.org/10.1179/mst.1989.5.9.865.

[39] C.B. Ponton, R.D. Rawlings, Mater. Sci. Technol. 5 (1989) 961–976, https://doi.org/10.1179/mst.1989.5.10.961.

[40] G.V. Samsonov, The Oxide Handbook, IFI/Plenum Press, New York, Washington, London (1973).

[41] T.A. Parthasarathy, R.A. Rapp, M. Opeka, M.K. Cinibulk, J. Am. Ceram. Soc. 95 (1) (2012) 338–349, https://doi.org/10.1111/j.1551-2916.2011.04927.x.

[42] P. Mogilevsky, M.K. Cinibulk, J. Am. Ceram. Soc. 107 (2) (2024) 1274–1301, https://doi.org/10.1111/jace.19471.